


Article

# Construction of Petal-Like Ag NWs@NiCoP with Three-Dimensional Core-Shell Structure for Overall Water Splitting

Fan Wang<sup>1</sup>, Rui Tian<sup>1</sup>, Xingzhong Guo<sup>1,2,\*</sup> , Yang Hou<sup>3</sup>, Chang Zou<sup>1</sup> and Hui Yang<sup>1</sup>

<sup>1</sup> State Key Laboratory of Silicon Materials, School of Materials Science and Engineering, Zhejiang University, Hangzhou 310027, China; 426698@zju.edu.cn (F.W.); tianr@zju.edu.cn (R.T.); 21926018@zju.edu.cn (C.Z.); yanghui@zju.edu.cn (H.Y.)

<sup>2</sup> Hangzhou Global Scientific and Technological Innovation Center, Zhejiang University, Hangzhou 311200, China

<sup>3</sup> Key Laboratory of Biomass Chemical Engineering of Ministry of Education, College of Chemical and Biological Engineering, Zhejiang University, Hangzhou 310027, China; yhou@zju.edu.cn

\* Correspondence: msewj01@zju.edu.cn

**Abstract:** High-efficiency, good electrical conductivity and excellent performance electrocatalysts are attracting growing attention in the field of overall water splitting. In order to achieve the desirable qualities, rational construction of the structure and chemical composition of electrocatalysts is of fundamental importance. Herein, petal-like structure Ni<sub>0.33</sub>Co<sub>0.67</sub>P shells grown on conductive silver nanowires (Ag NWs) cores as bifunctional electrocatalysts for overall water splitting were synthesized through a facile hydrothermal method and phosphorization. The resultant three-dimensional core-shell petal-like structure Ag NWs@Ni<sub>0.33</sub>Co<sub>0.67</sub>P possesses excellent catalytic activities in alkaline conditions with the overpotential of 259 mV for the oxygen evolution reaction (OER), 121 mV for the hydrogen evolution reaction (HER) and a full cell voltage of 1.64 V to reach the current density of 10 mA cm<sup>-2</sup>. Highly conductive Ag NWs as cores and high surface area petal-like Ni<sub>0.33</sub>Co<sub>0.67</sub>P as shells can endow outstanding catalytic performance for the bifunctional electrocatalyst. Thus, the synthetic strategy of the three-dimensional core-shell structure Ag NWs@Ni<sub>0.33</sub>Co<sub>0.67</sub>P considerably advances the practice of Ag NWs toward electrocatalysts.

**Keywords:** overall water splitting; core-shell structure; Ag NWs; transition metal phosphides; bifunctional electrocatalysts



**Citation:** Wang, F.; Tian, R.; Guo, X.; Hou, Y.; Zou, C.; Yang, H. Construction of Petal-Like Ag NWs@NiCoP with Three-Dimensional Core-Shell Structure for Overall Water Splitting. *Nanomaterials* **2022**, *12*, 1205. <https://doi.org/10.3390/nano12071205>

Academic Editor: Adriano Sacco

Received: 18 March 2022

Accepted: 31 March 2022

Published: 4 April 2022

**Publisher's Note:** MDPI stays neutral with regard to jurisdictional claims in published maps and institutional affiliations.



**Copyright:** © 2022 by the authors. Licensee MDPI, Basel, Switzerland. This article is an open access article distributed under the terms and conditions of the Creative Commons Attribution (CC BY) license (<https://creativecommons.org/licenses/by/4.0/>).

## 1. Introduction

The non-renewability of traditional fossil fuels and environmental issues have forced researchers to exploit more advanced renewable energy technologies to achieve cleaner energy production and conversion [1–3]. In this regard, electrochemical water splitting is a very promising approach for generating high-quality hydrogen fuel [4,5]. The products of electrolyzed water are hydrogen and oxygen, and the reaction has the characteristics of safety, no pollution and easy separation of products. Hydrogen is an ideal high-efficiency, zero-emission and sustainable clean energy [6]. The water splitting reaction consists of two half-reactions: the oxygen evolution reaction (OER) and the hydrogen evolution reaction (HER), both of which require efficient electrocatalysts to improve their performance [7,8]. Previous studies have found that noble metals have excellent catalytic properties for water electrolysis, but it is difficult to put them into actual industrial production based on cost considerations [9,10]. Silver materials, as a typical noble metal material, have been extensively studied as alternative conducting electrode materials in the electrochemical field, because they are inexpensive in relative comparison with those other noble metal materials [11,12]. In particular, silver nanowires (Ag NWs) are used in water electrolysis due to their high electrical conductivity, mechanical flexibility and facile synthesis [13,14].

Transition metals represented by Ni, Co and Fe have shown high catalytic activity in some studies [15–17]. Transition metal phosphides that feature distinct charge structures (positive charges in metal and negative charges in phosphorus) have been studied extensively because of their good catalytic properties [18,19]. In particular, NiCo phosphides have a wide application prospect because of their environmental friendliness, low cost and high electrocatalytic activity in water electrolysis. Ji et al. designed CoP nanoframe electrocatalysts, which presented bifunctional electrocatalytic reactivities for both HER and OER [20]. Ren et al. fabricated NiP/NF catalysts with excellent electrocatalytic activities and stability [21]. Lin et al. synthesized a unique CoP/NiCoP nanotadpole heterojunction structure with special morphology such as nanotadpoles, showing good HER activity over a wide pH range and with real seawater [22]. NiCo phosphides provide more diverse redox reactions and tunable interlayer space [23]. Besides, by growing on conductive substrates, NiCo phosphides help to enhance conductivity and improve charge-transfer features.

It is well known that the properties of a catalyst are significantly determined by its size, structure and morphology [19,24]. Accurate control of the electrocatalyst structure can effectively increase the surface areas and further reinforce the catalytic active sites, thereby improving the electrocatalytic performance [25,26]. Three-dimensional nanostructures have the advantages of large specific surface area, more active sites and rapid mass transmission, while one-dimensional nanowires and nanosheets suffer from low-speed electron transfer and slow electrolyte diffusion [27]. Therefore, it is necessary to effectively combine nanowires and nanosheets to form three-dimensional nanomaterials for improving electrocatalytic performance and stability. As a supporting conductive material, Ag NWs with outstanding physicochemical properties not only improve the conductivity of catalysts but also support nanosheets. By a synergistic combination of functional Ag NWs and transition metal phosphides to obtain a three-dimensional material with a core-shell structure, the electrocatalytic performance improves effectively. However, to the best of our knowledge, there are almost no reports on the application of Ag NWs composite transition metal phosphides to water splitting.

In this work, a well-designed three-dimensional core-shell petal-like Ag NWs@NiCoP architecture is synthesized by a simple hydrothermal procedure and phosphorization process. Based on the previous research of our group, appropriate Ag NWs were selected as the electrically conductive substrates to make sure that nanosheets would grow uniformly on the Ag NWs. The facile and efficient method fabricates three-dimensional core-shell Ag NWs@NiCoP with more active sites and outstanding electrical conductivity. Three-dimensional core-shell Ag NWs@NiCoP architecture electrocatalyst achieves enhanced electrocatalytic properties as a bifunctional catalyst, which endows core-shell petal-like Ag NWs@NiCoP architecture with the catalytic ability for overall water splitting.

## 2. Materials and Methods

### 2.1. Preparation of Three-Dimensional Core-Shell Petal-Like Ag NWs@Ni<sub>0.33</sub>Co<sub>0.67</sub>P

Preparation of three-dimensional core-shell petal-like Ag NWs@Ni<sub>0.33</sub>Co<sub>0.67</sub>-OH: Ag NWs were prepared using facile methods mentioned in a previous report [28]. The as-obtained Ag NWs (2 mL, 2 wt%) were dispersed in 25 mL of water ultrasonically. Next, 0.33 mmol of Ni(NO<sub>3</sub>)<sub>2</sub>·6H<sub>2</sub>O, 0.67 mmol of Co(NO<sub>3</sub>)<sub>2</sub>·6H<sub>2</sub>O, 2 mmol of NH<sub>4</sub>F and 4 mmol of urea were dissolved in 25 mL of Ag NWs suspension. After stirring for 30 min, the resulting solution was treated hydrothermally at 120 °C for 6 h in a Teflon-lined stainless-steel autoclave. After the autoclave was cooled down to room temperature, the products were obtained by centrifuge, washed several times with deionized water and subsequently freeze-dried. Multiple experiments were conducted concurrently every time in order to obtain enough samples.

Phosphorization of three-dimensional core-shell petal-like Ag NWs@Ni<sub>0.33</sub>Co<sub>0.67</sub>-OH: To prepare Ag NWs@Ni<sub>0.33</sub>Co<sub>0.67</sub>P electrode, 20 mg of Ag NWs@Ni<sub>0.33</sub>Co<sub>0.67</sub>-OH and 200 mg of NaH<sub>2</sub>PO<sub>2</sub> powders were placed separately in a porcelain crucible boat in a tube furnace at 350 °C for 2 h with a heating rate of 2 °C·min<sup>-1</sup> under an Ar atmosphere. Ag

NWs@Ni<sub>0.33</sub>Co<sub>0.67</sub>-OH was placed at the downstream side of the furnace. After cooling to room temperature, the three-dimensional core-shell petal-like Ag NWs@Ni<sub>0.33</sub>Co<sub>0.67</sub>P was obtained. For comparison, the molar ratios of Ni(NO<sub>3</sub>)<sub>2</sub>·6H<sub>2</sub>O to Co(NO<sub>3</sub>)<sub>2</sub>·6H<sub>2</sub>O were changed to be 1:1 and 2:1, and the as-obtained samples were named Ag NWs@Ni<sub>0.5</sub>Co<sub>0.5</sub>P and Ag NWs@Ni<sub>0.67</sub>Co<sub>0.33</sub>P. Ni<sub>0.33</sub>Co<sub>0.67</sub>P was prepared using the same method without the addition of Ag NWs.

## 2.2. Characterizations

Powder X-ray diffraction (XRD) patterns were processed using an Empyrean 200,895 X-ray diffractometer with Cu K $\alpha$  radiation (PANalytical, Almelo, Netherlands). The morphology was performed using scanning electron microscopy (SEM, Hitachi SU8010 (Hitachi, Tokyo, Japan)). Transmission electron microscopy (TEM) images were obtained on a Hitachi HT-7700 (Hitachi, Tokyo, Japan) equipped with an energy dispersive X-ray (EDX) spectrometer. High-resolution transmission electron microscopy (HRTEM) was recorded on a TEM (FEI Tecnai G2 F20 (Thermo Fisher Scientific, Waltham, MA, USA)). X-ray photoelectron spectroscopy (XPS) analyses were conducted on a Thermo Scientific K-Alpha (Thermo Fisher Scientific, Waltham, MA, USA). Inductively coupled plasma-mass spectrometry (ICP-MS) was carried out on an Agilent 7700 series (Agilent Technologies Inc., Santa Clara, CA, USA).

## 2.3. Electrochemical Measurements

All the electrochemical measurements were performed using a CHI760E workstation (Chenhua Corp., Shanghai, China) in 1.0 M KOH (pH = 13.9). Electrodes were prepared using the same methods previously mentioned in the literature [29]. The loading of catalysts was controlled to be about 2 mg·cm<sup>-2</sup>. As-prepared electrodes acted as the working electrode, while a Pt sheet served as the counter electrode and an Ag/AgCl electrode worked as the reference electrode. The potentials were corrected to the reversible hydrogen electrode (RHE) by the Nernst equation ( $E_{\text{RHE}} = E_{\text{Ag/AgCl}} + 0.059 \cdot \text{pH} + 0.197 \text{ V}$ ), in which  $E_{\text{Ag/AgCl}}$  is measured with the Ag/AgCl reference electrode. The main electrochemical tests included cyclic voltammetry (CV), linear sweep voltammetry (LSV) and electrochemical impedance spectroscopy (EIS). First of all, the obtained electrocatalysts were activated with the CV tests at a scan rate of 50 mV s<sup>-1</sup>. After activation, the LSV was conducted at a scan rate of 2 mV s<sup>-1</sup>, and the EIS was performed at 1.6 V (−0.15 V) versus RHE for OER (HER). Stability measurements were analyzed by 3000 cycles of CV tests and chronopotentiometry for 48 h. The electrochemical active surface area (ECSA) was estimated by CV at various scanning rates from 10 to 100 mV s<sup>-1</sup> in the non-faradaic region between −0.18 and −0.12 V (versus Ag/AgCl). Note that all results were calibrated by iR-compensation according to Equation (1):

$$E_{\text{result}} = E_{\text{RHE}} - i \cdot R_s, \quad (1)$$

where  $R_s$  was obtained from the EIS Nyquist plot. The catalytic activity of electrodes was calculated by the turnover frequency (TOF) with previously reported equations and methods [30].

## 3. Results and Discussion

### 3.1. Structure of Three-Dimensional Core-Shell Petal-Like Ag NWs@Ni<sub>0.33</sub>Co<sub>0.67</sub>P

The delicate processing strategy of the three-dimensional core-shell petal-like structure Ag NWs@Ni<sub>0.33</sub>Co<sub>0.67</sub>P is schematically indicated in Figure 1a–c. To fabricate the three-dimensional core-shell petal-like structure Ag NWs@Ni<sub>0.33</sub>Co<sub>0.67</sub>P, the Ag NWs@Ni<sub>0.33</sub>Co<sub>0.67</sub>-OH was firstly generated through a hydrothermal approach. The urea is decomposed in the aqueous solution to release CO<sub>3</sub><sup>2-</sup> and OH<sup>-</sup> anions, and subsequently the Co<sup>2+</sup> and Ni<sup>2+</sup> cations interact with the CO<sub>3</sub><sup>2-</sup> and OH<sup>-</sup> ions, after which plenty of nanosheets are uniformly arranged on the Ag NWs. SEM images demonstrate the diameter of smooth Ag NWs is approximately 90–120 nm (Figure 1a1 and Figure S1a), and Ni<sub>0.33</sub>Co<sub>0.67</sub>-OH nanosheets (Figure 1b1 and Figure S1b) with a diameter of around 300–400 nm are ho-

mogeneously and densely wrapped on the Ag NWs. The nanosheets are stacked and arranged in different directions to form a special three-dimensional core-shell petal-like structure [31]. During the whole heat treatment period, the entire structure can be phosphated owing to the unimpeded infiltration of phosphorus, forming an equally three-dimensional core-shell petal-like Ag NWs@Ni<sub>0.33</sub>Co<sub>0.67</sub>P structure with no collapse and aggregation (Figure 1c1 and Figure S1c). Besides, the effect of the molar ratios of Ni to Co precursor of the Ag NWs@NiCoP was investigated. From Figures S2 and S3, it can be seen that Ag NWs@Ni<sub>0.5</sub>Co<sub>0.5</sub>P and Ag NWs@Ni<sub>0.67</sub>Co<sub>0.33</sub>P still maintain the morphology of nanosheets grown on Ag NWs. With the increase of nickel content, the petal-like nanosheets disappear and gradually form hexagonal nanosheets.

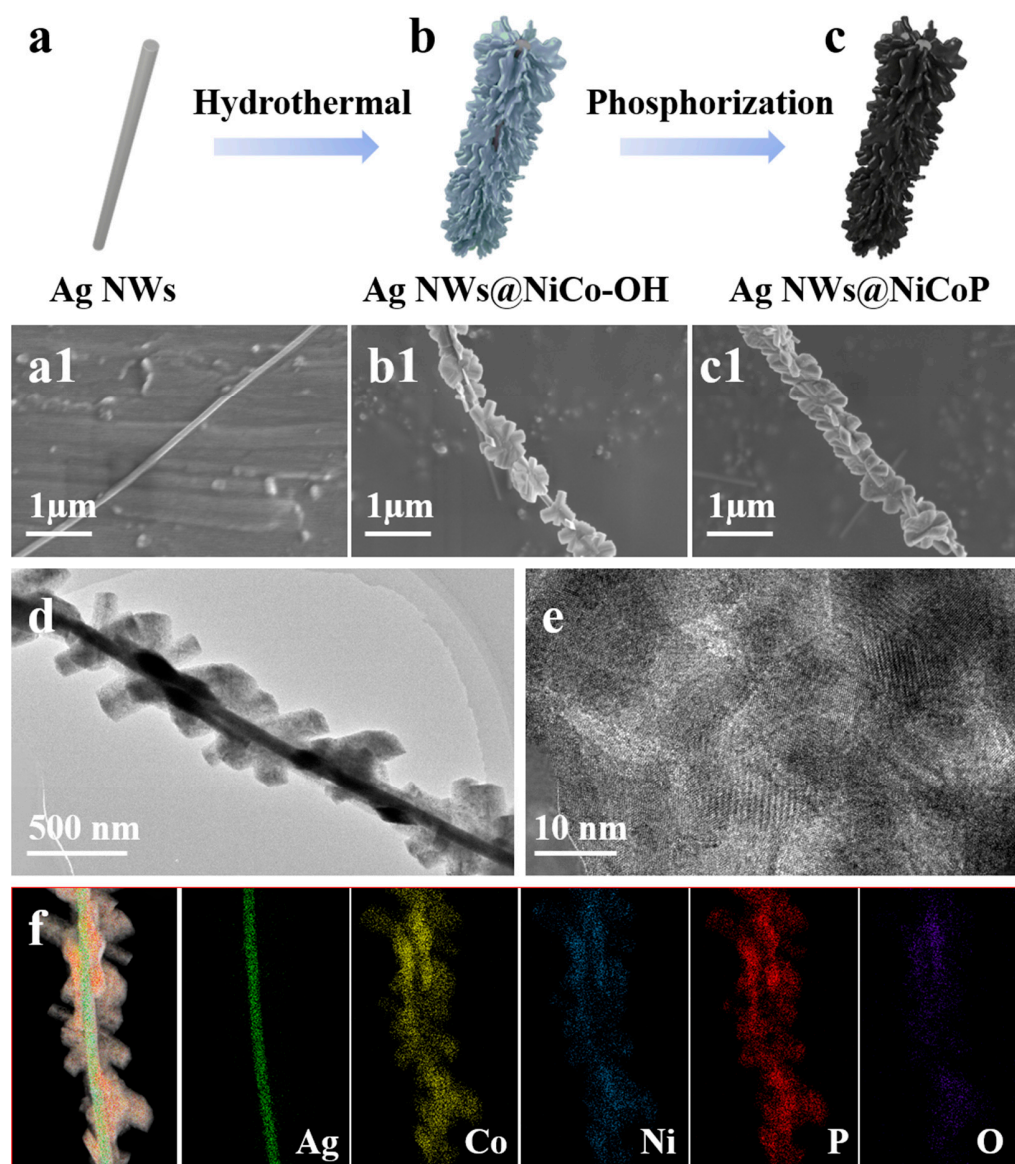


**Figure 1.** The synthesis procedures and the resulting structures for three-dimensional core-shell petal-like Ag NWs@Ni<sub>0.33</sub>Co<sub>0.67</sub>P: (a) Ag NWs, (a1) SEM image of Ag NWs, (b) Ag NWs@Ni<sub>0.33</sub>Co<sub>0.67</sub>-OH, (b1) SEM image of Ag NWs@Ni<sub>0.33</sub>Co<sub>0.67</sub>-OH, (c) Ag NWs@Ni<sub>0.33</sub>Co<sub>0.67</sub>P, (c1) SEM image of Ag NWs@Ni<sub>0.33</sub>Co<sub>0.67</sub>P, (d–e) TEM images of Ag NWs@Ni<sub>0.33</sub>Co<sub>0.67</sub>P and (f) elemental mapping of Ag NWs@Ni<sub>0.33</sub>Co<sub>0.67</sub>P.

Moreover, the three-dimensional core-shell petal-like structure Ag NWs@Ni<sub>0.33</sub>Co<sub>0.67</sub>P was further observed using TEM and HRTEM with the EDX spectrometer. Figure 1d depicts

that the surface of Ag NWs is homogeneously covered with the petal-like  $\text{Ni}_{0.33}\text{Co}_{0.67}\text{P}$  nanosheets. The (111), (210) and (201) crystal planes of NiCoP phase with the lattice spacing of 0.22, 0.191 and 0.202 nm are observed in the HRTEM images, which matches well with the XRD result (Figure 1e and Figure S4). Furthermore, the corresponding EDX mapping analysis was conducted to demonstrate the distribution of the elemental components of the Ag NWs@ $\text{Ni}_{0.33}\text{Co}_{0.67}\text{P}$  (Figure 1f). The results indicate the existence and distinct distribution of Ag, Co, Ni, P and O throughout the nanostructure, revealing the well-defined core-shell structure with Ag NWs cores and  $\text{Ni}_{0.33}\text{Co}_{0.67}\text{P}$  nanosheets.

XRD was conducted to elucidate the crystalline structure of the samples, as shown in Figure 2a and Figure S5. The intense peaks located at  $2\theta$  values of  $38.1^\circ$ ,  $44.2^\circ$ ,  $64.4^\circ$  and  $77.4^\circ$  are consistent with the Ag NWs corresponding to the (111), (200), (220) and (311) crystalline planes (PDF#04-0783) in all the curves [13]. During the hydrothermal process (Figure S5), the diffraction peaks at  $19.2^\circ$ ,  $38.6^\circ$  and  $52.2^\circ$  can be well identified as the respective (001), (011) and (012) planes of  $\text{Ni}(\text{OH})_2$  (PDF#73-1520) and the diffraction peaks located at  $17.6^\circ$ ,  $33.9^\circ$ ,  $35.5^\circ$  and  $39.5^\circ$  can be attributed to (020), (221), (040) and (231) planes of  $\text{Co}(\text{CO}_3)_{0.5}(\text{OH})\cdot 0.11\text{H}_2\text{O}$  (PDF#48-0083) [32]. It illuminates the successful fabrication of NiCo hydroxide on Ag NWs. After the phosphorization conversion, new diffraction peaks at about  $40.9^\circ$ ,  $47.5^\circ$ , and  $54.3^\circ$  emerge (Figure 2a), which can be indexed to (111), (210), and (300) planes of NiCoP (PDF#71-2336) [19]. In addition, Table S1 confirms the atomic ratios of Ni, Co, P and Ag in the Ag NWs@NiCoP with different Ni and Co ratios.

The chemical and electronic surface states of Ag NWs@ $\text{Ni}_{0.33}\text{Co}_{0.67}\text{P}$  were conducted by XPS (Figure S6). In the Ag 3d spectra, Figure 2b exhibits two peaks of Ag  $3d_{5/2}$  and Ag  $3d_{3/2}$  at the binding energies of 368 and 374 eV in Ag NWs@ $\text{Ni}_{0.33}\text{Co}_{0.67}\text{P}$ , respectively, indicating the typical peak of elemental Ag [11]. In comparison with the Ag NWs@ $\text{Ni}_{0.33}\text{Co}_{0.67}\text{-OH}$  (Figure S7a), the peak position of Ag NWs@ $\text{Ni}_{0.33}\text{Co}_{0.67}\text{P}$  generates a shift. In the Ni 2p spectra (Figure S7b), the peaks located at 855.93 and 862.06 eV are assigned to the  $\text{Ni}(\text{OH})_x$  and its satellite peak in the Ni  $2p_{3/2}$  spectra for Ag NWs@ $\text{Ni}_{0.33}\text{Co}_{0.67}\text{-OH}$  [33]. After phosphorization, in Figure 2c, the high-resolution Ni  $2p_{3/2}$  energy level of Ag NWs@ $\text{Ni}_{0.33}\text{Co}_{0.67}\text{P}$  exhibits three different chemical states with binding energies of 853.13, 856.74 and 861.21 eV associated with  $\text{Ni}^{x+}$  in NiCoP, oxidized Ni species, and the satellite of the Ni  $2p_{3/2}$  peak, respectively [34]. Similarly, the Co  $2p_{3/2}$  of the converted NiCoP (Figure 2d and Figure S7c) appears a new peak observed at 778.32 eV as a result of the formation of Co-P [33]. The Co  $2p_{3/2}$  spectra in Ag NWs@ $\text{Ni}_{0.33}\text{Co}_{0.67}\text{P}$  exhibit main peaks at 778.32, 781.85 and 784.96 eV, which correspond to Co species in NiCoP, oxidized Co species, and the satellite of the Co  $2p_{3/2}$  peak, respectively [35]. The other three peaks at 793.3, 797.93 and 802.47 eV accounted for the Co  $2p_{1/2}$  core level spectra, which are indexed to the Co species in NiCoP, the oxidized Co species and the satellite of the Co  $2p_{1/2}$  peak, respectively. In the P 2p spectra (Figure 2e), the peaks centered at 129.38 and 130.29 eV belong to the P  $2p_{3/2}$  and P  $2p_{1/2}$  in Ag NWs@ $\text{Ni}_{0.33}\text{Co}_{0.67}\text{P}$ , respectively, which are derived from NiCoP [36]. Moreover, the peak that appeared at 134.3 eV is likely to be originated from the oxidation of the samples' surface in the environment. Figure 2f displays the O 1s binding energy for Ag NWs@ $\text{Ni}_{0.33}\text{Co}_{0.67}\text{P}$  to further demonstrate the oxidized Ni and oxidized Co. The peak at 531.57 eV may indicate the presence of the Ni-O and Co-O bonds [37]. Meanwhile, the peak at 533.12 eV can be illustrated as the oxidized phosphate species.

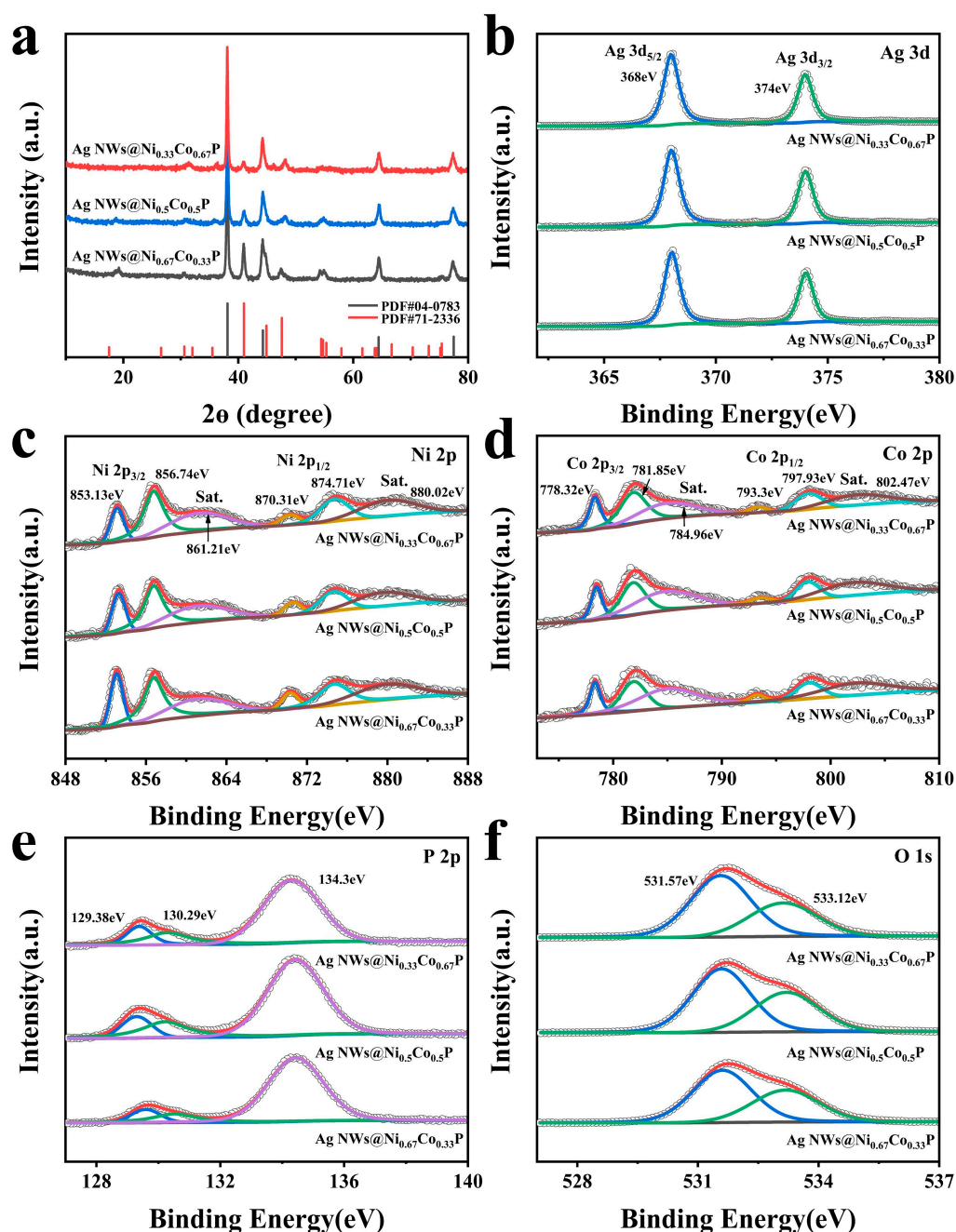


**Figure 2.** (a) XRD patterns of Ag NWs@NiCoP with different Ni and Co ratios. XPS spectra of Ag NWs@NiCoP with different Ni and Co ratios: (b) Ag 3d, (c) Ni 2p, (d) Co 2p, (e) P 2p, (f) O 1s.

### 3.2. Electrocatalytic Performance of Three-Dimensional Core-Shell Petal-Like Ag NWs@Ni<sub>0.33</sub>Co<sub>0.67</sub>P

A standard three-electrode system was used to evaluate the electrocatalytic OER and HER performances of the as-fabricated three-dimensional core-shell petal-like Ag NWs@Ni<sub>0.33</sub>Co<sub>0.67</sub>P. Meanwhile, the performance of bare nickel foam, IrO<sub>2</sub> and Pt/C were compared under identical measurement conditions.

Figure 3a shows the LSV curves for OER. The three-dimensional core-shell petal-like Ag NWs@Ni<sub>0.33</sub>Co<sub>0.67</sub>P reveals the highest OER performance, and the overpotentials are 259 and 332 mV at 10 and 100 mA·cm<sup>-2</sup>, respectively. The overpotential of Ag NWs@Ni<sub>0.33</sub>Co<sub>0.67</sub>P is smaller than Ag NWs, Ni<sub>0.33</sub>Co<sub>0.67</sub>P and IrO<sub>2</sub>. This is likely the result of the tight connection between Ag NW cores and Ni<sub>0.33</sub>Co<sub>0.67</sub>P shells that realizes rapid electron transfer and generates an intense synergistic effect. This synergistic effect exposes

more active sites and effectively improves the catalytic performance. In order to demonstrate the influence of NiCoP shells grown on Ag NWs cores, Ag NWs@NiCoP with different Ni and Co ratios were carried out. Ag NWs@Ni<sub>0.5</sub>Co<sub>0.5</sub>P and Ag NWs@Ni<sub>0.67</sub>Co<sub>0.33</sub>P require overpotentials of 264 and 273 mV to drive the current density of 10 mA·cm<sup>-2</sup>, respectively, illustrating that Ag NWs@Ni<sub>0.33</sub>Co<sub>0.67</sub>P is an active electrocatalyst. The OER activity of bare nickel foam as catalyst substrate is measured for reference (Figure S8), illustrating that the vast majority of electrocatalytic properties of the as-prepared electrode stem from Ag NWs@Ni<sub>0.33</sub>Co<sub>0.67</sub>P catalyst. Moreover, the high OER activity of Ag NWs@Ni<sub>0.33</sub>Co<sub>0.67</sub>P is higher than other recently reported OER electrocatalysts (Table S2). The lower overpotential of Ag NWs@Ni<sub>0.33</sub>Co<sub>0.67</sub>P illustrates that the OER performance of Ag NWs@Ni<sub>0.33</sub>Co<sub>0.67</sub>P exceeds other catalysts, which results from the three-dimensional core-shell structure and phosphorization. Figure 3b reveals the smallest Tafel slope (63 mV dec<sup>-1</sup>) of three-dimensional core-shell petal-like Ag NWs@Ni<sub>0.33</sub>Co<sub>0.67</sub>P, which is lower than Ag NWs@Ni<sub>0.5</sub>Co<sub>0.5</sub>P (65.8 mV dec<sup>-1</sup>), Ag NWs@Ni<sub>0.67</sub>Co<sub>0.33</sub>P (73.6 mV dec<sup>-1</sup>), Ni<sub>0.33</sub>Co<sub>0.67</sub>P (89.55 mV dec<sup>-1</sup>), Ag NWs (219.59 mV dec<sup>-1</sup>) and IrO<sub>2</sub> (91.66 mV dec<sup>-1</sup>), explaining that Ag NWs@Ni<sub>0.33</sub>Co<sub>0.67</sub>P proceeds with faster OER kinetics [38].

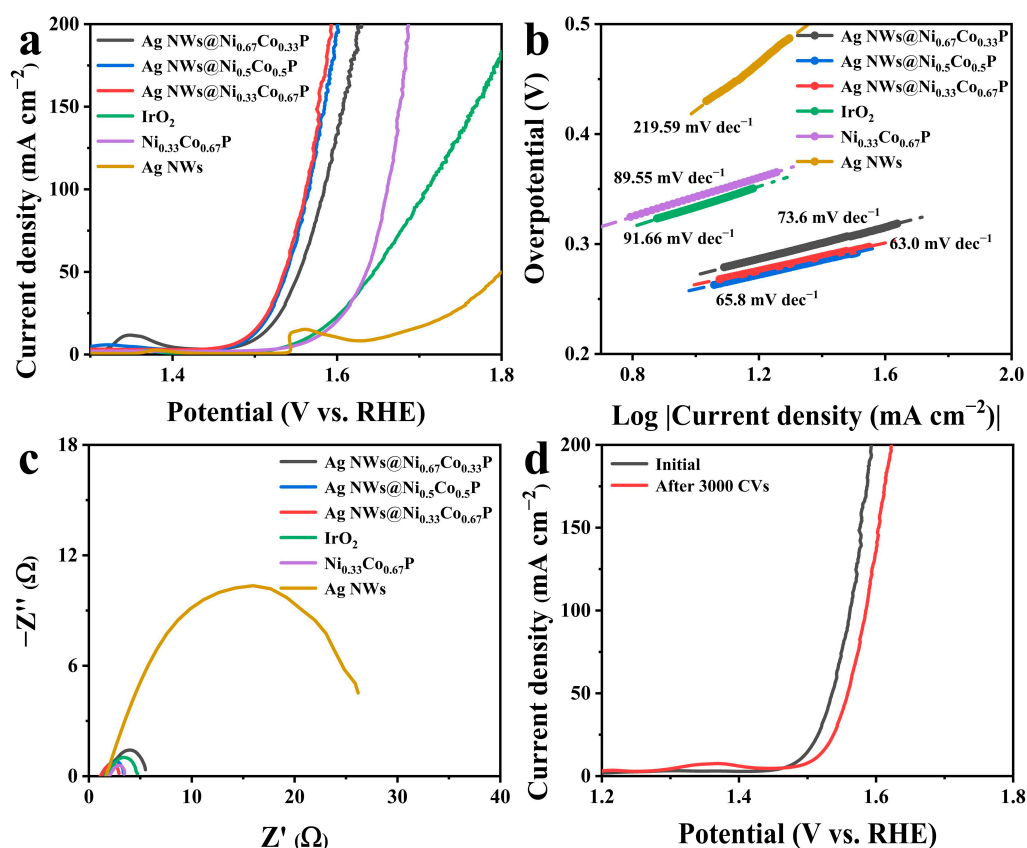


**Figure 3.** (a) LSV curves, (b) Tafel slopes and (c) Nyquist plots of Ag NWs@NiCoP with different Ni and Co ratios, Ni<sub>0.33</sub>Co<sub>0.67</sub>P, Ag NWs and IrO<sub>2</sub> for OER; (d) LSV curves initially and after 3000 cycles of CV of Ag NWs@Ni<sub>0.33</sub>Co<sub>0.67</sub>P for OER.

Furthermore, the charge transport capability of the Ag NWs@Ni<sub>0.33</sub>Co<sub>0.67</sub>P electrode was employed by electrochemical impedance spectroscopy (EIS). The semicircle diameter represents the charge-transfer resistance ( $R_{ct}$ ) and the horizontal intercept stands for the solution resistance ( $R_s$ ) [39,40]. The EIS results exhibit that three-dimensional core-shell petal-like Ag NWs@Ni<sub>0.33</sub>Co<sub>0.67</sub>P has the lowest  $R_{ct}$  among all the samples, which displays that the three-dimensional core-shell structure tremendously accelerates the electron transfer and has favorable reaction kinetics (Figure 3c) [41]. Simultaneously, to further clarify the advantages of phosphorization, a comparison test was conducted against the

electrocatalytic performance of Ag NWs@NiCo-OH (Figure S9), which turns out that Ag NWs@NiCoP possesses more excellent catalytic activity. To estimate the OER durability of the Ag NWs@Ni<sub>0.33</sub>Co<sub>0.67</sub>P, LSV curves after 3000 cycles of CV and the chronopotentiometry test were obtained from Figure 3d and Figure S10a. LSV curves of Ag NWs@Ni<sub>0.33</sub>Co<sub>0.67</sub>P acquired before and after cycles present imperceptible change, and the OER potentials are sustainable with a negligible potential loss after 48 h, confirming excellent stability of Ag NWs@Ni<sub>0.33</sub>Co<sub>0.67</sub>P for OER electrocatalysis. However, the OER reaction is normally accompanied by the conversion of metal phosphide to metal phosphate, manifesting in the change of morphology (Figure S10b) [42]. In reality, metal phosphates play a significant role in promoting catalytic activity and stabilizing catalytic reactions [33].

Next to the OER activity, the HER performance of the three-dimensional core-shell petal-like Ag NWs@Ni<sub>0.33</sub>Co<sub>0.67</sub>P electrode was also estimated with the same conditions. Figure 4a shows the LSV curves for all the samples and Pt/C, demonstrating that three-dimensional core-shell petal-like Ag NWs@Ni<sub>0.33</sub>Co<sub>0.67</sub>P has much higher HER performance than those of Ag NWs@Ni<sub>0.5</sub>Co<sub>0.5</sub>P, Ag NWs@Ni<sub>0.67</sub>Co<sub>0.33</sub>P, Ni<sub>0.33</sub>Co<sub>0.67</sub>P and Ag NWs. Ag NWs@Ni<sub>0.33</sub>Co<sub>0.67</sub>P needs an overpotential of 121 mV to reach the current density of 10 mA cm<sup>-2</sup>. Furthermore, another valuable method of the Tafel plot is often used to characterize kinetics and rate control steps of the catalytic process for evaluating HER activity. The Ag NWs@Ni<sub>0.33</sub>Co<sub>0.67</sub>P displays the lowest Tafel slope of 102.88 mV·dec<sup>-1</sup>, compared to Ag NWs@Ni<sub>0.5</sub>Co<sub>0.5</sub>P (103.38 mV dec<sup>-1</sup>), Ag NWs@Ni<sub>0.67</sub>Co<sub>0.33</sub>P (109.44 mV dec<sup>-1</sup>), Ni<sub>0.33</sub>Co<sub>0.67</sub>P (105.16 mV dec<sup>-1</sup>) and Ag NWs (123.33 mV dec<sup>-1</sup>) (Figure 4b). The overpotential of Pt/C is 17 mV at 10 mA cm<sup>-2</sup> with a Tafel slope of 14.06 mV·dec<sup>-1</sup>. As a blank control, the HER activity of bare nickel foam substrate was also measured (Figure S11), indicating the inert nature of HER in the range of applied potentials. In addition, the HER performance of other electrocatalysts was compared (Table S3), Ag NWs@Ni<sub>0.33</sub>Co<sub>0.67</sub>P has essentially excellent HER electrocatalytic activity.

The catalysts kinetics interface reactions of Ag NWs@Ni<sub>0.33</sub>Co<sub>0.67</sub>P was investigated by EIS in the electrocatalytic HER process. As expected (Figure 4c), the electron-transfer resistance of Ag NWs@Ni<sub>0.33</sub>Co<sub>0.67</sub>P is much lower than that of Ag NWs@Ni<sub>0.5</sub>Co<sub>0.5</sub>P and Ag NWs@Ni<sub>0.67</sub>Co<sub>0.33</sub>P, in accordance with the LSV curve and Tafel slope results. Compared with Ag NWs@NiCo-OH (Figure S12), Ag NWs@NiCoP describes much lower overpotential, smaller Tafel slope and lower R<sub>ct</sub>, which endows high active sites for HER. Moreover, Figure 4d and Figure S13a indicate that Ag NWs@Ni<sub>0.33</sub>Co<sub>0.67</sub>P shows an insignificant decrement in the potential after stability measurements. Besides, from the SEM images in Figure S13b, Ag NWs@Ni<sub>0.33</sub>Co<sub>0.67</sub>P after electrocatalysis retain the three-dimensional core-shell petal-like morphology, proving the robustness of the structure.

Inspired by the prominent activities of the electrodes as bifunctional catalysts in alkaline solution, Ag NWs@Ni<sub>0.33</sub>Co<sub>0.67</sub>P electrodes were used as both the anode and cathode in two-electrode overall water splitting to monitor their performance. As presented in Figure 5a, Ag NWs@Ni<sub>0.33</sub>Co<sub>0.67</sub>P | Ag NWs@Ni<sub>0.33</sub>Co<sub>0.67</sub>P achieves cell voltage of 1.64 and 1.84 V to drive the current density of 10 and 100 mA cm<sup>-2</sup>, respectively, which are higher than those of Ag NWs@Ni<sub>0.5</sub>Co<sub>0.5</sub>P and Ag NWs@Ni<sub>0.67</sub>Co<sub>0.33</sub>P. Meanwhile, the IrO<sub>2</sub> | | Pt/C cell voltages are 1.57 and 1.76 V, respectively. Interestingly, after the cell voltage reaches 1.93 V, the current density of the Ag NWs@Ni<sub>0.33</sub>Co<sub>0.67</sub>P | Ag NWs@Ni<sub>0.33</sub>Co<sub>0.67</sub>P exceeded that of the IrO<sub>2</sub> | | Pt/C. Besides, the Ag NWs@Ni<sub>0.33</sub>Co<sub>0.67</sub>P electrode used for overall water splitting is outperforming other reported bifunctional electrocatalysts (Table S4). More importantly, Figure S14 declares the voltage of Ag NWs@Ni<sub>0.33</sub>Co<sub>0.67</sub>P possesses a small increase over 48 h durability measurement at a current density of 10 mA·cm<sup>-2</sup>, proving good stability in the long-term electrocatalytic procedure.



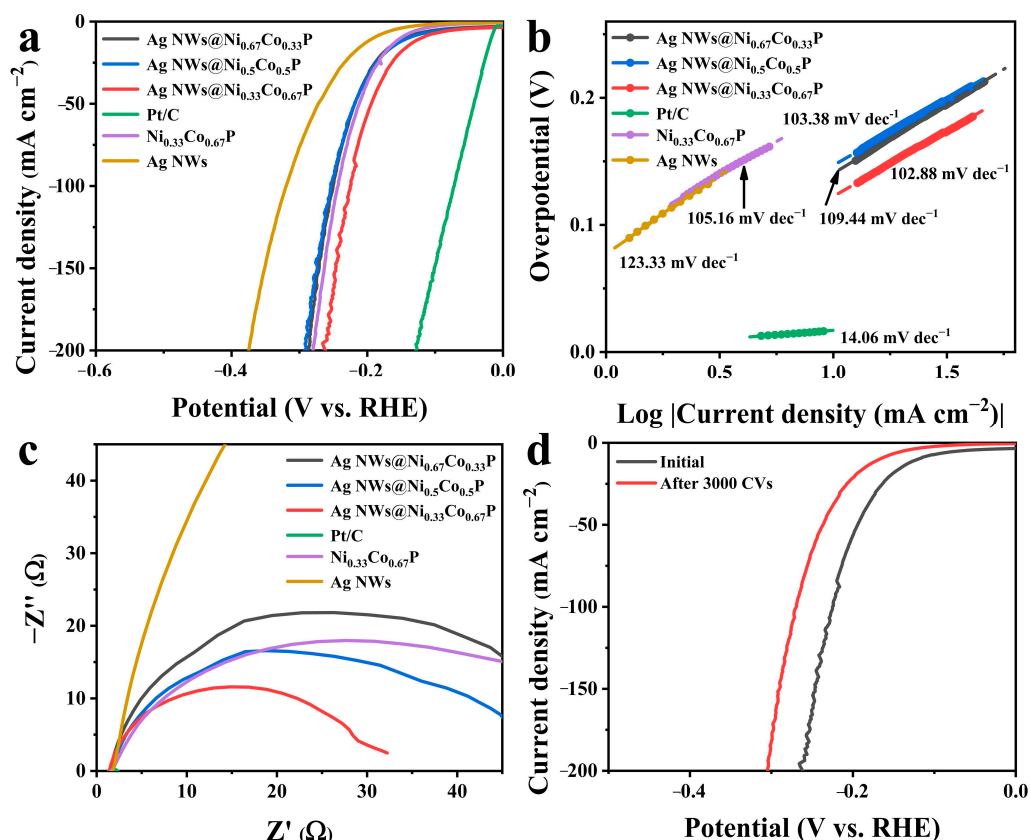


**Figure 4.** (a) LSV curves, (b) Tafel slopes and (c) Nyquist plots of Ag NWs@NiCoP with different Ni and Co ratios, Ni<sub>0.33</sub>Co<sub>0.67</sub>P, Ag NWs and Pt/C for HER; (d) LSV curves initially and after 3000 cycles of CV of Ag NWs@Ni<sub>0.33</sub>Co<sub>0.67</sub>P for HER.

The XPS was performed to illustrate the changes of Ag NWs@Ni<sub>0.33</sub>Co<sub>0.67</sub>P after stability tests (Figure S15). Compared with the HER stability test, the intense anodic oxidation in the OER stability test leads to a distinct and irreversible phase transformation of metal phosphides to metal oxides/oxyhydroxides with the morphology change of Ag NWs@Ni<sub>0.33</sub>Co<sub>0.67</sub>P [38]. In reality, the useful active sites of metal phosphides for OER were confirmed to be the metal oxides/oxyhydroxides formed during the OER operation [33]. Obviously, after OER stability measurement, the lower binding energy Ni (853.13 eV) and Co (778.32 eV) peaks disappear, which are attributed to Ni-P and Co-P in the as-fabricated Ag NWs@Ni<sub>0.33</sub>Co<sub>0.67</sub>P. This result explains the phase transformation of metal phosphides to metal oxides/oxyhydroxides, which enables the supply of more active sites to facilitate catalytic reaction [43]. From Figure S15c, the lower binding energy peaks disappear in the P 2p spectra after the OER stability test, suggesting that the metal phosphides have been oxidized to metal oxides [44]. This phase transformation can be further demonstrated by the appearance of a new peak after the OER stability test (Figure S15d). The new peak at 529.4 eV in the O 1s spectra corresponds well to the M-O species, which is testified as representative electrocatalytic phases for reactivities [38]. Overall, the in situ formed metal oxides/oxyhydroxides during the OER process can be regarded as the electrocatalytically active phase.

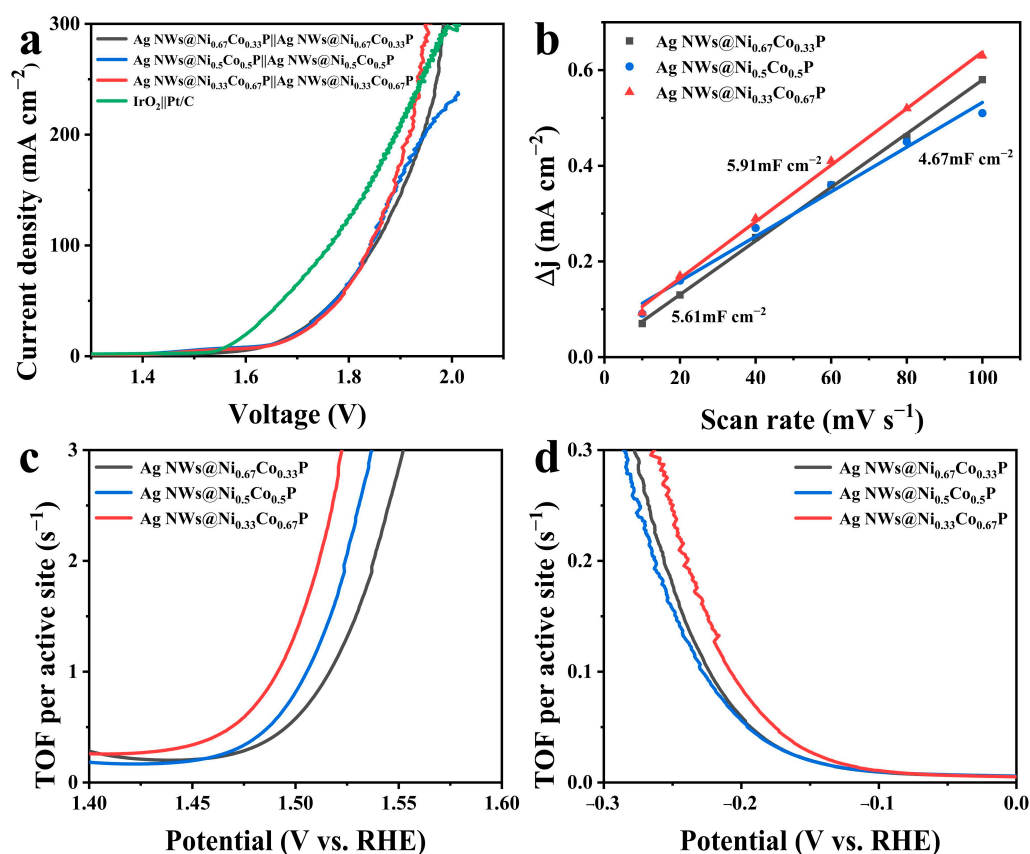


**Figure 5.** (a) Polarization curves of the Ag NWs@NiCoP || Ag NWs@NiCoP cell with different Ni and Co ratios and the IrO<sub>2</sub> || Pt/C cell for overall water splitting. (b) Plots of the current density versus the various scan rates for Ag NWs@NiCoP with different Ni and Co ratios; TOF curves of Ag NWs@NiCoP with different Ni and Co ratios for (c) OER and (d) HER.

The double-layer capacitance ( $C_{dl}$ ) estimates the relative ECSA via a CV test with various scan rates. Large ECSA with more exposed active sites can achieve better electrocatalytic activity [20]. Figure S16 depicts the CV curves of Ag NWs@NiCoP at different scan rates. Apparently, calculating the slope values of the current density versus the scan speed shows that Ag NWs@Ni<sub>0.33</sub>Co<sub>0.67</sub>P obtains the biggest  $C_{dl}$ . The increased order of  $C_{dl}$  is Ag NWs@Ni<sub>0.5</sub>Co<sub>0.5</sub>P (4.67 mF·cm<sup>-2</sup>) < Ag NWs@Ni<sub>0.67</sub>Co<sub>0.33</sub>P (5.61 mF·cm<sup>-2</sup>) < Ag NWs@Ni<sub>0.33</sub>Co<sub>0.67</sub>P (5.91 mF·cm<sup>-2</sup>), illustrating that the specific surface area is available enhanced by reasonably designing the three-dimensional core-shell structure. Meanwhile, the TOF of the catalysts evaluates the intrinsic catalytic activity of OER and HER processes [45]. Figure S17 reveals the number of active sites was calculated by CV tests with a scan rate of 50 mV·s<sup>-1</sup> in 1 M phosphate buffer solution (pH = 7). Figure 5c describes the TOF value of Ag NWs@Ni<sub>0.33</sub>Co<sub>0.67</sub>P as 3.85 s<sup>-1</sup> at 1.53 V for OER, which is higher than that of Ag NWs@Ni<sub>0.5</sub>Co<sub>0.5</sub>P (2.47 s<sup>-1</sup>) and Ag NWs@Ni<sub>0.67</sub>Co<sub>0.33</sub>P (1.54 s<sup>-1</sup>). Furthermore, for HER (Figure 5d), the TOF value of Ag NWs@Ni<sub>0.33</sub>Co<sub>0.67</sub>P at -0.2 V is 0.086 s<sup>-1</sup>, whereas the TOFs of Ag NWs@Ni<sub>0.5</sub>Co<sub>0.5</sub>P and Ag NWs@Ni<sub>0.67</sub>Co<sub>0.33</sub>P are 0.056 and 0.060 s<sup>-1</sup>, respectively. The biggest TOF value of Ag NWs@Ni<sub>0.33</sub>Co<sub>0.67</sub>P for OER and HER processes available and distinctly confirmed the good catalytic activity.

The outstanding electrocatalytic performances of three-dimensional core-shell petal-like structure Ag NWs@Ni<sub>0.33</sub>Co<sub>0.67</sub>P can be assigned to the following factors: (1) three-dimensional core-shell structure generates a larger specific surface area and abundant active sites, leading to promoted electron transport and open channels for the effective release of gas; (2) the metallic nature of Ag NWs and Ni<sub>0.33</sub>Co<sub>0.67</sub>P enhance the electrical conductivity thus favors fast electron transport; (3) the intense synergistic effect between the three-dimensional core-shell structure of Ni<sub>0.33</sub>Co<sub>0.67</sub>P nanosheets and Ag NWs exposes

more active sites; (4) three-dimensional core-shell structure available to reduce the electron transport resistance between the  $\text{Ni}_{0.33}\text{Co}_{0.67}\text{P}$  shells and Ag NWs cores, thus improving the charge-transfer ability and catalytic activity.

#### 4. Conclusions

In summary, a three-dimensional core-shell petal-like structure Ag NWs@NiCoP as a bifunctional electrocatalyst was developed for overall water electrolysis. The excellent electrocatalytic performance of Ag NWs@NiCoP is attributed to its advantageous structural and chemical compositional design that results in strengthened electrical conductivity and facile electron transport. A three-dimensional core-shell structure constructed by one-dimensional Ag NWs and NiCoP nanosheets has the advantages of quick-speed electron transmission and fast diffusion of electrolytes. The as-constructed three-dimensional core-shell petal-like structure Ag NWs@NiCoP exhibits favorable catalytic performance for OER and HER. The use of Ag NWs@NiCoP as a bifunctional electrocatalyst will markedly simplify electrode preparation and facilitate its extensive application. This method provides a novel strategy for the synthesis of three-dimensional core-shell electrocatalysts by the combination of transition metal phosphide and Ag NWs.

**Supplementary Materials:** The following supporting information can be downloaded at: <https://www.mdpi.com/article/10.3390/nano12071205/s1>, Figure S1: SEM images of (a) Ag NWs, (b) Ag NWs@ $\text{Ni}_{0.33}\text{Co}_{0.67}\text{-OH}$  and (c) Ag NWs@ $\text{Ni}_{0.33}\text{Co}_{0.67}\text{P}$ ; Figure S2: SEM images of (a, b) Ag NWs@ $\text{Ni}_{0.5}\text{Co}_{0.5}\text{-OH}$  and (c, d) Ag NWs@ $\text{Ni}_{0.5}\text{Co}_{0.5}\text{P}$ ; Figure S3: SEM images of (a, b) Ag NWs@ $\text{Ni}_{0.67}\text{Co}_{0.33}\text{-OH}$  and (c, d) Ag NWs@ $\text{Ni}_{0.67}\text{Co}_{0.33}\text{P}$ ; Figure S4: HRTEM images of Ag NWs@ $\text{Ni}_{0.33}\text{Co}_{0.67}\text{P}$ : (a) (111), (b) (210), (c) (201); Figure S5: XRD patterns of Ag NWs@NiCo-OH with different Ni and Co ratios; Figure S6: Overall X-ray photoelectron spectroscopy (XPS) spectra of (a) Ag NWs@NiCoP and (b) Ag NWs@NiCo-OH with different Ni and Co ratios; Figure S7: XPS spectra of Ag NWs@NiCo-OH with different Ni and Co ratios: (a) Ag 3d, (b) Ni 2p, (c) Co 2p, and (d) O 1s; Figure S8: (a) LSV, (b) the corresponding Tafel slope and (c) Nyquist plot of nickel foam towards OER; Figure S9: (a) LSV curves, (b) the corresponding Tafel plots and (c) Nyquist plots of Ag NWs@NiCo-OH with different Ni and Co ratios towards OER; Figure S10: (a) Chronopotentiometry test of Ag NWs@ $\text{Ni}_{0.33}\text{Co}_{0.67}\text{P}$  for OER and (b) SEM images of Ag NWs@ $\text{Ni}_{0.33}\text{Co}_{0.67}\text{P}$  after 48 h chronopotentiometry test towards OER; Figure S11: (a) LSV, (b) the corresponding Tafel slope and (c) Nyquist plot of nickel foam towards HER; Figure S12: (a) LSV curves, (b) the corresponding Tafel plots and (c) Nyquist plots of Ag NWs@NiCo-OH with different Ni and Co ratios towards HER; Figure S13: (a) Chronopotentiometry test of Ag NWs@ $\text{Ni}_{0.33}\text{Co}_{0.67}\text{P}$  for HER and (b) SEM images of Ag NWs@ $\text{Ni}_{0.33}\text{Co}_{0.67}\text{P}$  after 48 h chronopotentiometry test towards HER; Figure S14: Chronopotentiometry test of Ag NWs@ $\text{Ni}_{0.33}\text{Co}_{0.67}\text{P}$  for overall water splitting; Figure S15: XPS spectra of (a) Ni 2p, (b) Co 2p, (c) P 2p and (d) O 1s of Ag NWs@ $\text{Ni}_{0.33}\text{Co}_{0.67}\text{P}$  before test, after HER stability test and after OER stability test; Figure S16: CV curves of (a) Ag NWs@ $\text{Ni}_{0.67}\text{Co}_{0.33}\text{P}$ , (b) Ag NWs@ $\text{Ni}_{0.5}\text{Co}_{0.5}\text{P}$ , and (c) Ag NWs@ $\text{Ni}_{0.33}\text{Co}_{0.67}\text{P}$  at different scan rates (10, 20, 40, 60, 80 and 100  $\text{mV S}^{-1}$ ) in the non-faradaic potential region of -0.18 to -0.12 V vs. Ag/AgCl; Figure S17: CV curves of Ag NWs@NiCoP with different Ni and Co ratios at a scan rate of 50  $\text{mV S}^{-1}$  in 1.0 M PBS (pH = 7) for (a) OER and (b) HER; Table S1: Metal elements content detected by ICP-MS analysis.; Table S2: Comparison of the OER performances of Ag NWs@ $\text{Ni}_{0.33}\text{Co}_{0.67}\text{P}$  with the previously reported electrocatalysts at alkaline media; Table S3: Comparison of the HER performances of Ag NWs@ $\text{Ni}_{0.33}\text{Co}_{0.67}\text{P}$  with the previously reported electrocatalysts at alkaline media; Table S4: Comparison of overall water splitting performances of Ag NWs@ $\text{Ni}_{0.33}\text{Co}_{0.67}\text{P}$  with the previously reported electrocatalysts at alkaline media. References [46–61] are cited in the Supplementary Materials.

**Author Contributions:** Formal analysis, R.T. and C.Z.; Methodology, H.Y.; Writing—original draft, F.W.; Writing—review and editing, X.G. and Y.H. All authors have read and agreed to the published version of the manuscript.

**Funding:** This research was funded by the National Natural Science Foundation of China, grant number 21875217; 51372225; and the Open Project Fund of State Key Laboratory of Silicon Materials, grant number SKL2019-04.

**Institutional Review Board Statement:** Not applicable.

**Informed Consent Statement:** Not applicable.

**Data Availability Statement:** The data presented in this study are available in this article.

**Conflicts of Interest:** The authors declare no conflict of interest.

## References

1. Luo, X.; Ji, P.; Wang, P.; Cheng, R.; Chen, D.; Lin, C.; Zhang, J.; He, J.; Shi, Z.; Li, N.; et al. Interface Engineering of Hierarchical Branched Mo-Doped Ni<sub>3</sub>S<sub>2</sub>/Ni<sub>x</sub>P<sub>y</sub> Hollow Heterostructure Nanorods for Efficient Overall Water Splitting. *Adv. Energy Mater.* **2020**, *10*, 1903891. [[CrossRef](#)]
2. Meena, A.; Thangavel, P.; Nissimagoudar, A.S.; Singh, A.N.; Jana, A.; Jeong, D.S.; Im, H.; Kim, K.S. Bifunctional oxovanadate doped cobalt carbonate for high-efficient overall water splitting in alkaline-anion-exchange-membrane water-electrolyzer. *Chem. Eng. J.* **2022**, *430*, 132623. [[CrossRef](#)]
3. Wang, N.; Ning, S.; Yu, X.; Chen, D.; Li, Z.; Xu, J.; Meng, H.; Zhao, D.; Li, L.; Liu, Q.; et al. Graphene composites with Ru-RuO<sub>2</sub> heterostructures: Highly efficient Mott-Schottky-type electrocatalysts for pH-universal water splitting and flexible zinc-air batteries. *Appl. Catal. B* **2022**, *302*, 120838. [[CrossRef](#)]
4. Luo, W.; Wang, Y.; Luo, L.; Gong, S.; Wei, M.; Li, Y.; Gan, X.; Zhao, Y.; Zhu, Z.; Li, Z. Single-Atom and Bimetallic Nanoalloy Supported on Nanotubes as a Bifunctional Electrocatalyst for Ultrahigh-Current-Density Overall Water Splitting. *ACS Catal.* **2022**, *12*, 1167–1179. [[CrossRef](#)]
5. Kenanakis, G.; Vernardou, D.; Dalamagkas, A.; Katsarakis, N. Photocatalytic and electrooxidation properties of TiO<sub>2</sub> thin films deposited by sol-gel. *Catal. Today* **2015**, *240*, 146–152. [[CrossRef](#)]
6. Zhang, H.; Maijenburg, A.W.; Li, X.; Schweizer, S.L.; Wehrspohn, R.B. Bifunctional Heterostructured Transition Metal Phosphides for Efficient Electrochemical Water Splitting. *Adv. Funct. Mater.* **2020**, *30*, 2003261. [[CrossRef](#)]
7. Jiang, W.J.; Tang, T.; Zhang, Y.; Hu, J.S. Synergistic Modulation of Non-Precious-Metal Electrocatalysts for Advanced Water Splitting. *Acc. Chem. Res.* **2020**, *53*, 1111–1123. [[CrossRef](#)]
8. Guo, L.; Liu, Q.; Liu, Y.; Chen, Z.; Jiang, Y.; Jin, H.; Zhou, T.; Yang, J.; Liu, Y. Self-supported tremella-like MoS<sub>2</sub>-AB particles on nickel foam as bifunctional electrocatalysts for overall water splitting. *Nano Energy* **2022**, *92*, 106707. [[CrossRef](#)]
9. Ji, X.; Lin, Y.; Zeng, J.; Ren, Z.; Lin, Z.; Mu, Y.; Qiu, Y.; Yu, J. Graphene/MoS<sub>2</sub>/FeCoNi(OH)<sub>x</sub> and Graphene/MoS<sub>2</sub>/FeCoNiP<sub>x</sub> multilayer-stacked vertical nanosheets on carbon fibers for highly efficient overall water splitting. *Nat. Commun.* **2021**, *12*, 1380. [[CrossRef](#)]
10. Wu, L.; Yu, L.; Zhang, F.; McElhenny, B.; Luo, D.; Karim, A.; Chen, S.; Ren, Z. Heterogeneous Bimetallic Phosphide Ni<sub>2</sub>P-Fe<sub>2</sub>P as an Efficient Bifunctional Catalyst for Water/Seawater Splitting. *Adv. Funct. Mater.* **2020**, *31*, 2006484. [[CrossRef](#)]
11. Chala, S.A.; Tsai, M.C.; Su, W.N.; Ibrahim, K.B.; Thirumalraj, B.; Chan, T.S.; Lee, J.F.; Dai, H.; Hwang, B.J. Hierarchical 3D architected Ag nanowires shelled with NiMn-layered double hydroxide as an efficient bifunctional oxygen electrocatalyst. *ACS Nano* **2020**, *14*, 1770–1782. [[CrossRef](#)] [[PubMed](#)]
12. Zhao, M.; Wang, Y.; Zhao, Q.; Li, Q.; Pang, H. Facile synthesis of silver nanowire-zeolitic imidazolate framework 67 composites as high-performance bifunctional oxygen catalysts. *Nanoscale* **2018**, *10*, 15755–15762. [[CrossRef](#)] [[PubMed](#)]
13. Liu, Y.; Zhang, G.; Zuo, C.; Zhao, K.; Zeng, J.; Yin, J.; Chen, H.; Xie, S.; Qiu, Y. Core-Shell AgNWs@Ni(OH)<sub>2</sub> Nanowires Anchored on Filter Paper for Efficient Hydrogen Evolution Reaction. *J. Electrochem. Soc.* **2020**, *167*, 116520. [[CrossRef](#)]
14. Zhang, X.; Marianov, A.N.; Jiang, Y.; Cazorla, C.; Chu, D. Hierarchically constructed silver nanowire@nickel-iron layered double hydroxide nanostructures for electrocatalytic water splitting. *ACS Appl. Nano Mater.* **2019**, *3*, 887–895. [[CrossRef](#)]
15. Sun, D.; Lin, S.; Yu, Y.; Liu, S.; Meng, F.; Du, G.; Xu, B. One-pot synthesis of N and P Co-doped carbon layer stabilized cobalt-doped MoP 3D porous structure for enhanced overall water splitting. *J. Alloy. Compd.* **2022**, *895*, 162595. [[CrossRef](#)]
16. Wang, P.; Wang, T.; Qin, R.; Pu, Z.; Zhang, C.; Zhu, J.; Chen, D.; Feng, D.; Kou, Z.; Mu, S.; et al. Swapping Catalytic Active Sites from Cationic Ni to Anionic S in Nickel Sulfide Enables More Efficient Alkaline Hydrogen Generation. *Adv. Energy Mater.* **2022**, *210*, 3359. [[CrossRef](#)]
17. Suryanto, B.H.R.; Wang, Y.; Hocking, R.K.; Adamson, W.; Zhao, C. Overall electrochemical splitting of water at the heterogeneous interface of nickel and iron oxide. *Nat. Commun.* **2019**, *10*, 5599. [[CrossRef](#)]
18. Zhao, Y.; Dongfang, N.; Triana, C.A.; Huang, C.; Erni, R.; Wan, W.; Li, J.; Stoian, D.; Pan, L.; Zhang, P.; et al. Dynamics and control of active sites in hierarchically nanostructured cobalt phosphide/chalcogenide-based electrocatalysts for water splitting. *Energy Environ. Sci.* **2022**. [[CrossRef](#)]
19. Du, C.; Yang, L.; Yang, F.; Cheng, G.; Luo, W. Nest-like NiCoP for Highly Efficient Overall Water Splitting. *ACS Catal.* **2017**, *7*, 4131–4137. [[CrossRef](#)]
20. Ji, L.; Wang, J.; Teng, X.; Meyer, T.J.; Chen, Z. CoP Nanoframes as Bifunctional Electrocatalysts for Efficient Overall Water Splitting. *ACS Catal.* **2019**, *10*, 412–419. [[CrossRef](#)]
21. Ren, J.; Hu, Z.; Chen, C.; Liu, Y.; Yuan, Z. Integrated Ni<sub>2</sub>P nanosheet arrays on three-dimensional Ni foam for highly efficient water reduction and oxidation. *J. Energy Chem.* **2017**, *26*, 1196–1202. [[CrossRef](#)]
22. Lin, Y.; Sun, K.; Liu, S.; Chen, X.; Cheng, Y.; Cheong, W.C.; Chen, Z.; Zheng, L.; Zhang, J.; Li, X.; et al. Construction of CoP/NiCoP Nanotadpoles Heterojunction Interface for Wide pH Hydrogen Evolution Electrocatalysis and Supercapacitor. *Adv. Energy Mater.* **2019**, *9*, 1901213. [[CrossRef](#)]

23. Yang, T.; Ye, Q.; Liang, Y.; Wu, L.; Long, X.; Xu, X.; Wang, F. Graded holey Nickel Cobalt layered double hydroxide nanosheet array electrode with high mass loading for high-energy-density all-solid-state supercapacitors. *J. Power Sources* **2020**, *449*, 227590. [[CrossRef](#)]
24. Li, M.; Zhao, Z.; Xia, Z.; Luo, M.; Zhang, Q.; Qin, Y.; Tao, L.; Yin, K.; Chao, Y.; Gu, L.; et al. Exclusive Strain Effect Boosts Overall Water Splitting in PdCu/Ir Core/Shell Nanocrystals. *Angew. Chem. Int. Ed. Engl.* **2021**, *60*, 8243–8250. [[CrossRef](#)]
25. Patil, S.J.; Chodankar, N.R.; Hwang, S.-K.; Shinde, P.A.; Raju, G.S.R.; Ranjith, K.S.; Huh, Y.S.; Han, Y.-K. Co-metal-organic framework derived CoSe<sub>2</sub>@MoSe<sub>2</sub> core-shell structure on carbon cloth as an efficient bifunctional catalyst for overall water splitting. *Chem. Eng. J.* **2022**, *429*, 132379. [[CrossRef](#)]
26. Jeong, S.; Mai, H.D.; Nam, K.H.; Park, C.M.; Jeon, K.J. Self-Healing Graphene-Templated Platinum-Nickel Oxide Heterostructures for Overall Water Splitting. *ACS Nano* **2022**, *16*, 930–938. [[CrossRef](#)]
27. Yu, L.; Zhu, Q.; Song, S.; McElhenny, B.; Wang, D.; Wu, C.; Qin, Z.; Bao, J.; Yu, Y.; Chen, S.; et al. Non-noble metal-nitride based electrocatalysts for high-performance alkaline seawater electrolysis. *Nat. Commun.* **2019**, *10*, 5106. [[CrossRef](#)]
28. Yang, H.; Chen, T.; Wang, H.; Bai, S.; Guo, X. One-pot rapid synthesis of high aspect ratio silver nanowires for transparent conductive electrodes. *Mater. Res. Bull.* **2018**, *102*, 79–85. [[CrossRef](#)]
29. Liao, H.; Guo, X.; Hou, Y.; Liang, H.; Zhou, Z.; Yang, H. Construction of defect-rich Ni-Fe-doped K<sub>0.23</sub>MnO<sub>2</sub> cubic nanoflowers via etching prussian blue analogue for efficient overall water splitting. *Small* **2020**, *16*, e1905223. [[CrossRef](#)]
30. Wang, F.; Guo, X.; He, F.; Hou, Y.; Liu, F.; Zou, C.; Yang, H. Binder free construction of hollow hierarchical Mn-Co-P nanoarrays on nickel foam as an efficient bifunctional electrocatalyst for overall water splitting. *Sustain. Energy Fuels* **2022**, *6*, 851–860. [[CrossRef](#)]
31. Bao, F.; Zhang, Z.; Guo, W.; Liu, X. Facile synthesis of three dimensional NiCo<sub>2</sub>O<sub>4</sub>@MnO<sub>2</sub> core-shell nanosheet arrays and its supercapacitive performance. *Electrochim. Acta* **2015**, *157*, 31–40. [[CrossRef](#)]
32. Jin, W.; Chen, J.; Wu, H.; Zang, N.; Li, Q.; Cai, W.; Wu, Z. Interface engineering of oxygen-vacancy-rich NiCo<sub>2</sub>O<sub>4</sub>/NiCoP heterostructure as an efficient bifunctional electrocatalyst for overall water splitting. *Catal. Sci. Technol.* **2020**, *10*, 5559–5565. [[CrossRef](#)]
33. Liang, H.; Gandi, A.N.; Anjum, D.H.; Wang, X.; Schwingenschlogl, U.; Alshareef, H.N. Plasma-Assisted Synthesis of NiCoP for Efficient Overall Water Splitting. *Nano Lett.* **2016**, *16*, 7718–7725. [[CrossRef](#)]
34. Boppella, R.; Tan, J.; Yang, W.; Moon, J. Homologous CoP/NiCoP Heterostructure on N-Doped Carbon for Highly Efficient and pH-Universal Hydrogen Evolution Electrocatalysis. *Adv. Funct. Mater.* **2018**, *29*, 1807976. [[CrossRef](#)]
35. Ma, B.; Yang, Z.; Chen, Y.; Yuan, Z. Nickel cobalt phosphide with three-dimensional nanostructure as a highly efficient electrocatalyst for hydrogen evolution reaction in both acidic and alkaline electrolytes. *Nano Res.* **2018**, *12*, 375–380. [[CrossRef](#)]
36. Zhao, D.; Zhao, R.; Dong, S.; Miao, X.; Zhang, Z.; Wang, C.; Yin, L. Alkali-induced 3D crinkled porous Ti<sub>3</sub>C<sub>2</sub> MXene architectures coupled with NiCoP bimetallic phosphide nanoparticles as anodes for high-performance sodium-ion batteries. *Energy Environ. Sci.* **2019**, *12*, 2422–2432. [[CrossRef](#)]
37. Lu, M.; Li, L.; Chen, D.; Li, J.; Klyui, N.I.; Han, W. MOF-derived nitrogen-doped CoO@CoP arrays as bifunctional electrocatalysts for efficient overall water splitting. *Electrochim. Acta* **2020**, *330*, 135210. [[CrossRef](#)]
38. Zhang, H.; Li, X.; Hähnel, A.; Naumann, V.; Lin, C.; Azimi, S.; Schweizer, S.L.; Maijenburg, A.W.; Wehrspohn, R.B. Bifunctional Heterostructure Assembly of NiFe LDH Nanosheets on NiCoP Nanowires for Highly Efficient and Stable Overall Water Splitting. *Adv. Funct. Mater.* **2018**, *28*, 1706847. [[CrossRef](#)]
39. Zhang, F.; Pei, Y.; Ge, Y.; Chu, H.; Craig, S.; Dong, P.; Cao, J.; Ajayan, P.M.; Ye, M.; Shen, J. Controlled synthesis of eutectic NiSe/Ni<sub>3</sub>Se<sub>2</sub> self-supported on Ni foam: An excellent bifunctional electrocatalyst for overall water splitting. *Adv. Mater. Interfaces* **2018**, *5*, 1701507. [[CrossRef](#)]
40. Xing, Y.; Li, D.; Li, L.; Tong, H.; Jiang, D.; Shi, W. Accelerating water dissociation kinetic in Co<sub>9</sub>S<sub>8</sub> electrocatalyst by mn/N Co-doping toward efficient alkaline hydrogen evolution. *Int. J. Hydrogen Energy* **2021**, *46*, 7989–8001. [[CrossRef](#)]
41. Xu, H.; Jia, H.; Fei, B.; Ha, Y.; Li, H.; Guo, Y.; Liu, M.; Wu, R. Charge transfer engineering via multiple heteroatom doping in dual carbon-coupled cobalt phosphides for highly efficient overall water splitting. *Appl. Catal. B* **2020**, *268*, 118404. [[CrossRef](#)]
42. Liang, Z.; Zhou, W.; Gao, S.; Zhao, R.; Zhang, H.; Tang, Y.; Cheng, J.; Qiu, T.; Zhu, B.; Qu, C.; et al. Fabrication of hollow CoP/TiO<sub>x</sub> heterostructures for enhanced oxygen evolution reaction. *Small* **2020**, *16*, e1905075. [[CrossRef](#)] [[PubMed](#)]
43. Li, J.; Yan, M.; Zhou, X.; Huang, Z.-Q.; Xia, Z.; Chang, C.-R.; Ma, Y.; Qu, Y. Mechanistic Insights on Ternary Ni<sub>2-x</sub>Co<sub>x</sub>P for Hydrogen Evolution and Their Hybrids with Graphene as Highly Efficient and Robust Catalysts for Overall Water Splitting. *Adv. Funct. Mater.* **2016**, *26*, 6785–6796. [[CrossRef](#)]
44. Qiu, B.; Cai, L.; Wang, Y.; Lin, Z.; Zuo, Y.; Wang, M.; Chai, Y. Fabrication of Nickel-Cobalt Bimetal Phosphide Nanocages for Enhanced Oxygen Evolution Catalysis. *Adv. Funct. Mater.* **2018**, *28*, 1706008. [[CrossRef](#)]
45. Liu, F.; Guo, X.; Hou, Y.; Wang, F.; Zou, C.; Yang, H. Hydrothermal combined with electrodeposition construction of a stable Co<sub>9</sub>S<sub>8</sub>/Ni<sub>3</sub>S<sub>2</sub>@NiFe-LDH heterostructure electrocatalyst for overall water splitting. *Sustain. Energy Fuels* **2021**, *5*, 1429–1438. [[CrossRef](#)]
46. Liu, X.; Wang, R.; He, Y.; Ni, Z.; Su, N.; Guo, R.; Zhao, Y.; You, J.; Yi, T. Construction of alternating layered quasi-three-dimensional electrode Ag NWs/CoO for water splitting: A discussion of catalytic mechanism. *Electrochim. Acta* **2019**, *317*, 468–477. [[CrossRef](#)]
47. He, P.; Yu, X.Y.; Lou, X.W. Carbon-Incorporated Nickel-Cobalt Mixed Metal Phosphide Nanoboxes with Enhanced Electrocatalytic Activity for Oxygen Evolution. *Angew. Chem. Int. Ed. Engl.* **2017**, *56*, 3897–3900. [[CrossRef](#)]

48. Hu, E.; Feng, Y.; Nai, J.; Zhao, D.; Hu, Y.; Lou, X.W. Construction of hierarchical Ni-Co-P hollow nanobricks with oriented nanosheets for efficient overall water splitting. *Energy Environ. Sci.* **2018**, *11*, 872–880. [[CrossRef](#)]
49. Bao, J.; Liu, W.; Xie, J.; Xu, L.; Guan, M.; Lei, F.; Zhao, Y.; Huang, Y.; Xia, J.; Li, H. Ni<sub>x</sub>Co<sub>3-x</sub>O<sub>4</sub> nanoneedle arrays grown on Ni foam as an efficient bifunctional electrocatalyst for full water splitting. *Chem. Asian J.* **2019**, *14*, 480–485. [[CrossRef](#)]
50. Jadhav, H.S.; Lim, A.C.; Roy, A.; Seo, J.G. Room-Temperature Ultrafast Synthesis of NiCo-Layered Double Hydroxide as an Excellent Electrocatalyst for Water Oxidation. *ChemistrySelect* **2019**, *4*, 2409–2415. [[CrossRef](#)]
51. Zhang, J.; Bai, X.; Wang, T.; Xiao, W.; Xi, P.; Wang, J.; Gao, D.; Wang, J. Bimetallic Nickel Cobalt Sulfide as Efficient Electrocatalyst for Zn-Air Battery and Water Splitting. *Nanomicro Lett.* **2019**, *11*, 1–13. [[CrossRef](#)] [[PubMed](#)]
52. Cong, M.; Sun, D.; Zhang, L.; Ding, X. In situ assembly of metal-organic framework-derived N-doped carbon/Co/CoP catalysts on carbon paper for water splitting in alkaline electrolytes. *Chin. J. Catal.* **2020**, *41*, 242–248. [[CrossRef](#)]
53. He, D.; Wu, X.; Liu, W.; Lei, C.; Yu, C.; Zheng, G.; Pan, J.; Lei, L.; Zhang, X. Co<sub>1-x</sub>S embedded in porous carbon derived from metal organic framework as a highly efficient electrocatalyst for oxygen evolution reaction. *Chin. Chem. Lett.* **2019**, *30*, 229–233. [[CrossRef](#)]
54. Qin, J.-F.; Lin, J.-H.; Chen, T.-S.; Liu, D.-P.; Xie, J.-Y.; Guo, B.-Y.; Wang, L.; Chai, Y.-M.; Dong, B. Facile synthesis of V-doped CoP nanoparticles as bifunctional electrocatalyst for efficient water splitting. *J. Energy Chem.* **2019**, *39*, 182–187. [[CrossRef](#)]
55. Tolstoy, V.P.; Lobinsky, A.A.; Kaneva, M.V. Features of inorganic nanocrystals formation in conditions of successive ionic layers deposition in water solutions and the Co(II)Co(III) 2D layered double hydroxide synthesis. *J. Mol. Liq.* **2019**, *282*, 32–38. [[CrossRef](#)]
56. Zou, W.; Dou, K.; Jiang, Q.; Xiang, J.; Kaun, C.-C.; Tang, H. Nearly spherical CoP nanoparticle/carbon nanosheet hybrids: A high-performance trifunctional electrocatalyst for oxygen reduction and water splitting. *RSC Adv.* **2019**, *9*, 39951–39957. [[CrossRef](#)]
57. Tie, J.; Han, J.; Diao, G.; Liu, J.; Xie, Z.; Cheng, G.; Sun, M.; Yu, L. Controllable synthesis of hierarchical nickel cobalt sulfide with enhanced electrochemical activity. *Appl. Surf. Sci.* **2018**, *435*, 187–194. [[CrossRef](#)]
58. Yan, J.; Chen, L.; Liang, X. Co<sub>9</sub>S<sub>8</sub> nanowires@NiCo LDH nanosheets arrays on nickel foams towards efficient overall water splitting. *Sci. Bull.* **2019**, *64*, 158–165. [[CrossRef](#)]
59. Jiang, B.; Li, Z. MOF-derived Co, Ni, Mn co-doped N-enriched hollow carbon for efficient hydrogen evolution reaction catalysis. *J. Solid State Chem.* **2021**, *295*, 121912. [[CrossRef](#)]
60. Sun, X.; Shao, Q.; Pi, Y.; Guo, J.; Huang, X. A general approach to synthesise ultrathin NiM (M = Fe, Co, Mn) hydroxide nanosheets as high-performance low-cost electrocatalysts for overall water splitting. *J. Mater. Chem. A* **2017**, *5*, 7769–7775. [[CrossRef](#)]
61. Yang, C.; Zhang, J.; Gao, G.; Liu, D.; Liu, R.; Fan, R.; Gan, S.; Wang, Y.; Wang, Y. 3D metallic Ti@Ni<sub>0.85</sub>Se with triple hierarchy as high-efficiency electrocatalyst for overall water splitting. *ChemSusChem* **2019**, *12*, 2271–2277. [[CrossRef](#)] [[PubMed](#)]